Optics Letters

X-ray-based overlay metrology using reciprocal space slicing analysis

JIAHAO ZHANG,[1] **XIUGUO CHEN,**[1,2,*] **TIANJUAN YANG,**[1] AND **SHIYUAN LIU**[1,2]

[1] *State Key Laboratory of Intelligent Manufacturing Equipment and Technology, Huazhong University of Science and Technology, Wuhan 430074, China*
[2] *Optics Valley Laboratory, Wuhan 430074, China*
**xiuguochen@hust.edu.cn*

Received 7 September 2023; revised 31 October 2023; accepted 2 November 2023; posted 3 November 2023; published 5 December 2023

Overlay serves as the pivotal performance indicator for lithography tools, and its prompt and precise measurement significantly underpins the process yield control. At present, diffraction-based overlay metrology employing optical wavelengths encounters constraints in terms of measurement sensitivity. When transitioning to x-ray wavelengths, the critical-dimension small-angle x-ray scattering (CDSAXS) method for nanostructure characterization necessitates reciprocal space mapping (RSM) and inverse problem solving, resulting in substantial throughput constraints. In this work, we propose an x-ray-based overlay metrology using reciprocal space slicing analysis (RSS), yielding high-precision overlay measurement at one single angle of incidence (AOI). Moreover, we examine the robustness of the proposed method against errors stemming from overlay target grating fabrication and measurement processes, substantiating its efficacy as a novel x-ray-based overlay metrology and unveiling the potential application of x-ray-based techniques within the realm of integrated circuit metrology. © 2023 Optica Publishing Group

https://doi.org/10.1364/OL.505346

Presently, semiconductor components such as memory and logic central processing units are meticulously constructed in a layer-by-layer manner, involving a repetitive sequence of lithography, etching, and deposition stages. The term “overlay” denotes the lateral displacement of the pattern that has been lithographically exposed and developed within a particular layer, concerning a pre-existing underlying structure present in another layer. At present, the degree of overlay precision achieved in high-end manufacturing ranges from 1 to 2 nm, with overlay metrology demanding a precision level in the range of 0.1 to 0.2 nm [1,2]. The measurement and meticulous control of the overlay between consecutive lithography steps constitute a critical undertaking in high-volume semiconductor manufacturing.

To address the heightened precision demands for the overlay control in semiconductor devices, diffraction-based overlay metrology has made substantial advancements [3]. Some researchers have observed that the difference between ±1st-order diffraction intensities, denoted as ΔI, demonstrates an approximately linear response to the overlay between the upper and lower layers of the grating within a confined range [4,5]. Furthermore, investigations have revealed that by utilizing the zeroth-order Mueller matrix within the multi-spectral Mueller matrix ellipsometer, a linear association emerges between the overlay and the combination of the off-diagonal-block Mueller matrix elements [6,7]. Nonetheless, the majority of these techniques rely on visible wavelengths. With the ongoing reduction in critical dimensions of nanostructures, the interconnected influence among parameters will curtail their applicability, leading to a corresponding decline in the sensitivity of these methodologies [8].

Confronted with these challenges, the integrated circuit industry is actively developing metrology based on x-ray techniques, capitalizing on x-ray wavelengths that are notably smaller than the feature size and exhibit high sensitivity to compositional alterations [9]. Among these methodologies, critical-dimension small-angle x-ray scattering (CDSAXS) stands out [10]. This technique already demonstrates the capability to reconstruct the cross-sectional profile of spacer-assisted quadruple patterning, displaying commendable concordance with transmission electron microscopy data [11]. However, CDSAXS utilizes reciprocal space mapping (RSM), which requires multiple angles of incidence (AOIs) scanning to acquire a subset of the sample’s reciprocal space and solves the inverse problem to extract parameters of the nanostructures, imposing a substantial throughput limitation [12]. At present, there are only few studies focusing on x-ray-based overlay metrology. Note that these studies also use RSM and discover the change in the position of the minimum value of the intensity shows a linear relationship with the overlay [13].

In this Letter, we introduce a novel concept for x-ray-based overlay metrology using reciprocal space slicing analysis (RSS). Compared with the traditional RSM, the RSS method involves measuring the scattering pattern at only one solitary AOI, which allows drastically simplified experimental procedure and faster assessment while ensuring the same accuracy as RSM [14]. We formulated a linear correlation connecting the combination of x-ray scattering intensities and overlay, ascertained the most favorable experimental configurations by minimizing the error in overlay measurements. Moreover, we executed simulations to evaluate the potential influence of errors stemming from overlay target grating fabrication and experimental measurement processes under the optimal configurations. Our outcomes provide compelling evidence for the effectiveness of this method

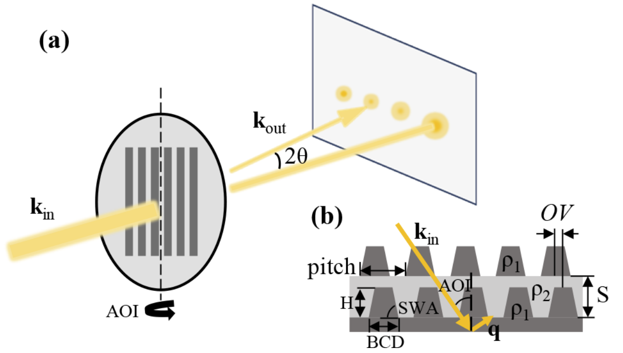

Fig. 1. (a) Schematic of the basic system layout for CDSAXS, where $\mathbf{k}_{in}$ and $\mathbf{k}_{out}$ denote the wave vectors of the incidence and scattering x-rays, respectively. (b) Cross section of the overlay target grating.

as a highly precise and robust approach for conducting overlay metrology.

Working Principle. Fig. 1 depicts a schematic illustration outlining the fundamental principles of CDSAXS [15]. Collimated monochromatic x-rays impinge upon the overlay target grating, positioned at an angle of incidence denoted as AOI. The detector captures multiple scattering orders occurring within a small-angle range due to elastic scattering, where 2θ denotes the scattering angle. The cross-sectional view of the overlay target grating is presented in Fig. 1(b), where the upper and lower nanostructures are symmetric trapezoids with the same profile and electron density ρ_1, the lateral shift is labelled as OV, and the thickness and electron density of the layer are designated as S and ρ_2, respectively. The scattering vector $\mathbf{q}$ corresponds to the vector difference between the incidence wave vector and the scattering wave vector, i.e., $\mathbf{q} = \mathbf{k}_{out} - \mathbf{k}_{in}$. Based on Eq. (1), the scattering vector $\mathbf{q}$ is transformed into the coordinate system of the sample [11]:

$$\begin{cases} q_x = |\mathbf{q}| \cos\left(AOI + \dfrac{2\theta}{2}\right) \\ q_z = |\mathbf{q}| \sin\left(AOI + \dfrac{2\theta}{2}\right) \end{cases}. \tag{1}$$

The form factor of the overlay target grating corresponds to the Fourier transform of the electron density distribution [11]. Subsequently, the scattering intensity is expressed as the square of the modulus of this form factor, as defined in Eq. (2):

$$\begin{gathered} F(q_x, q_z) = (\Delta\rho_1 + \Delta\rho_2 e^{-i(q_x \cdot OV + q_z S)})F_{\text{trap}} \\ I(q_x, q_z) = |F(q_x, q_z)|^2, \end{gathered} \tag{2}$$

where F_{trap} is the form factor of the trapezoidal cross section, the electron density differences are $\Delta\rho_1 = \rho_1 - \rho_2$ and $\Delta\rho_2 = \rho_1$.

RSS embodies a slice of the sample's reciprocal space, which encapsulates asymmetric details of the sample in scattering attributes (e.g., alterations in the intensity or positioning of the scattering order). Overlay, a lateral asymmetry factor, showcases a linear relationship with the relative fluctuations in scattering intensity which is mathematically expressed as

$$\frac{I_{OV}(q_x, q_z) - I_0(q_x, q_z)}{I_0(q_x, q_z)} = K(\Delta\rho_1, \Delta\rho_2, q_x, q_z, S) \cdot OV, \tag{3}$$

where $I_0(q_x, q_z)$ denotes the scattering intensity with $OV = 0$. On the right side of Eq. (1), K is only related to the parameters in parentheses and independent of the specific cross section. Detailed derivation of K is presented in Section 1 of Supplement 1.

The actual overlay target produced in manufacturing cannot achieve a perfect zero overlay, rendering the acquisition of $I_0(q_x, q_z)$ as prescribed in Eq. (3) unfeasible. To ensure the independence of overlay measurement from specific cross-sectional profiles, a solution akin to other diffraction-based overlay metrology is adopted. This involves introducing a set of designed shifts ±d to the overlay target. Equation (3) is then applied to these shifts ±d, resulting in the following equation:

$$\begin{cases} \dfrac{I_{OV+d}(q_x, q_z) - I_d(q_x, q_z)}{I_d(q_x, q_z)} = K_1(\Delta\rho_1, \Delta\rho_2, q_x, q_z, S, d) \cdot OV \\ \dfrac{I_{OV-d}(q_x, q_z) - I_{-d}(q_x, q_z)}{I_{-d}(q_x, q_z)} = K_2(\Delta\rho_1, \Delta\rho_2, q_x, q_z, S, -d) \cdot OV \end{cases}. \tag{4}$$

To derive the overlay OV from the aforementioned equation, an additional equation is required. By referencing the scattering intensity modeling formula Eq. (2), a distinct relationship between the scattering intensities at +d and −d becomes evident:

$$\frac{I_d(q_x, q_z)}{I_{-d}(q_x, q_z)} = K_3(\Delta\rho_1, \Delta\rho_2, q_x, q_z, S, d), \tag{5}$$

where comprehensive derivations from K_1 to K_3 are available in Section 1 of Supplement 1. Note that the calculation of the scattering intensity ratio K_3, obtained by dividing $I_d(q_x, q_z)$ by $I_{-d}(q_x, q_z)$, is based on modeling rather than measurement. By relying on the previously mentioned Eqs. (4) and (5), the overlay can be definitively expressed through the ensuing equation:

$$OV = \frac{I_{OV+d}(q_x, q_z) - K_3 I_{OV-d}(q_x, q_z)}{K_1 K_3 I_{OV-d}(q_x, q_z) - K_2 I_{OV+d}(q_x, q_z)}. \tag{6}$$

Results and discussion. Figure 1 (b) displays a schematic diagram detailing the overlay target grating in simulation. This structure consists of upper and lower silicon gratings, separated by a silicon dioxide layer in the center. The upper and lower silicon gratings share an identical, symmetrical cross section, characterized by a pitch of 125 nm. The bottom critical dimension (BCD), height (H), and sidewall angle (SWA) are defined as 80 nm, 100 nm, and 80°, respectively. The silicon dioxide layer possesses a thickness of 150 nm, while the designed shift is set as d = 20 nm. Note that in other overlay target gratings, especially when replacing the upper silicon grating with photoresist and adding bottom anti-reflective coating, only the electron density differences and layer thickness in Eq. (3) need to be adjusted, which does not affect the results of this proposed method. In addition, the Poisson noise has been added to make simulated scattering intensities more realistic, where we assume a background $I_{bk} = 10$ and the calculation is detailed in [12].

When provided with a specific set of cross-sectional parameters for the overlay target, variations in the AOI can introduce discrepancies in the accuracy of Eq. (3), consequently influencing the precision of the overlay measurement as per Eq. (6). Consequently, an optimization of the AOI is imperative to attain the utmost accuracy in the overlay measurement [16]. Owing to the superior signal-to-noise ratio exhibited by the 1st diffraction order, the intensity variation of this order is selected for the overlay metrology in this study. When employing the mean squared error between the input and measured overlay as the evaluation metric and the genetic algorithm as the optimization

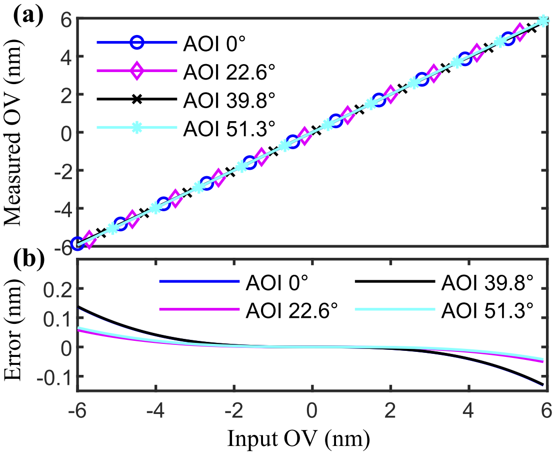

Fig. 2. (a) Comparison between the input and the measured overlay at optimal AOI settings and (b) the corresponding overlay measurement errors.

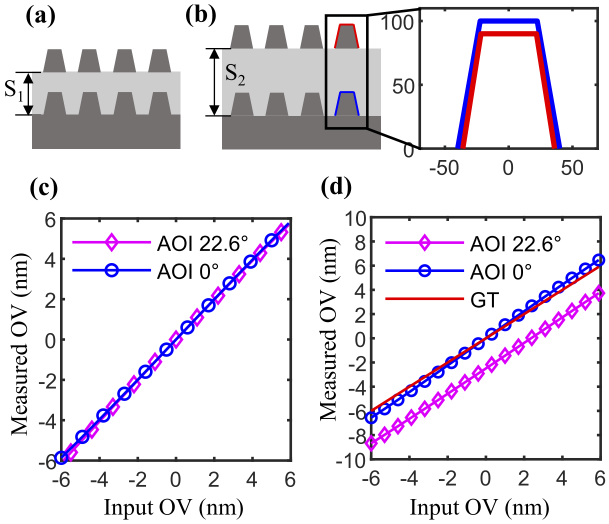

Fig. 3. Schematic of the overlay target grating without error (a) and with errors in silicon dioxide filling layer thickness and cross-sectional errors (b). The corresponding measured overlay with errors in silicon dioxide filling layer thickness (c) and cross-sectional errors (d).

algorithm, multiple local optima are obtained. Recognizing the substantial impact on x-ray absorption by the sample substrate at larger AOI, this study exclusively presents optimized AOI below 60°—specifically, 0°, 22.6°, 39.8°, and 51.3°. The measured overlay corresponding to these angles are showcased in Fig. 2. Evidently, a notable congruence exists between the input overlay and the measured values. In these optimal settings, the measured overlay exhibits a maximum relative error of merely 2.5%, as shown in Fig. 2(b), demonstrating the efficacy and precision of this overlay metrology method.

Beyond the optimal overlay measurement accuracy, this study investigates the robustness against overlay target grating deformations associated with upper and lower silicon grating cross sections and errors in the thickness of the silicon dioxide filling layer (as depicted in Fig. 3).

Compared with the overlay target grating without error in Fig. 3(a), we introduce a 10 nm error in the silicon dioxide filling layer thickness and 10% cross-sectional parameter errors between the upper and lower silicon gratings, as depicted in Fig. 3(b). To facilitate comprehension, the measured overlay results at AOI = 0° and 22.6° are presented in Figs. 3(c) and 3(d) (additional outcomes are available in Supplement 1 for different settings). Upon synthesizing Figs. 3 and Figs. S1 and S2 in Supplement 1, errors in the thickness of the silicon dioxide filling layer exhibit only a minor impact on the measured overlay, while in the presence of cross-sectional fabrication discrepancies, a difference emerges between the linear expression of the measured overlay and the ground truth (GT), which is more pronounced at larger AOI. Nonetheless, the measured overlay continues to manifest a linear association with the input overlay (as shown in Table S1 in Supplement 1), and deviations can potentially be calibrated through alternative techniques. One feasible approach is to use SEM or TEM to measure several pairs of overlay target gratings containing cross-sectional errors to calibrate the linear relationship, thereby expanding the application scope of the proposed method.

Moreover, this method demonstrates robustness against variations in the AOI. Keeping the overlay fixed at 5 nm and adjusting the AOI within the optimized settings of ±1° yields a maximum relative error within 5%, as shown in Fig. S3 in Supplement 1, indicating commendable precision in the overlay measurement. Similar to the effects of cross-sectional errors mentioned earlier, measurements conducted at larger AOI result in heightened inaccuracies. At a large AOI, in accordance with Eq. (1), the q_z component of the scattering vector increases. As a result, errors in the z direction of the sample (comprising the height of the silicon grating cross section and the thickness of the silicon dioxide layer), when multiplied by q_z, contribute to the perturbation of accuracy in the approximative formula.

Opting for a designed shift of the overlay target grating holds the potential to enhance the accuracy of this method [17]. Configure the overlay at values of 3 nm, 5 nm, and 8 nm, respectively. As an illustration, consider the overlay measurement at the AOI = 0° under different designed shifts, as depicted in Fig. S4 in Supplement 1. An insightful finding emerges: by setting the designed shift to 62.5 nm, equivalent to half of the pitch, the method attains its utmost accuracy. Specifically, for an overlay within 8 nm, a consistent measurement error of <2% is attainable. Conversely, prevailing diffraction-based overlay metrology necessitates wider linear ranges relative to the overlay and meticulous control of the designed shift within the overlay target grating, markedly amplifying implementation complexities. Within this approach, as per Eq. (5), the proportional correlation between the scattering intensities of the overlay target grating incorporating the designed shift (±d) is related to a limited set of parameters that are independent of the cross section, which can be precisely delineated. Consequently, securing a linear overlay relationship within the nanometer range emerges as the sole prerequisite, thus alleviating overlay target grating processing intricacies and improving the method's viability.

It is also worth pointing out that the scattering intensity of the overlay sample could be greatly enhanced due to its inherent characteristics of multilayer structures. Within the effective longitudinal coherence length, the scattering intensity scales with the second power of both the sample thickness [18,19] and electron density. In practice, the top of the overlay target may be developed by photoresist, which may lead to reduced scattering intensity due to its relatively lower electron density. This reduction can be offset by increasing the height of the photoresist grating layer and optimizing the thickness of the filling layer between the top and bottom gratings. Furthermore, the development of high aspect ratio structures like 3D NAND and DRAM offers the potential to optimize the overlay target by increasing the height of the gratings. Consequently, optimizing the design of the overlay target could give rise to a one to two orders of magnitude increase in the scattering intensity [20], which is another benefit of the proposed x-ray-based overlay metrology.

Currently, the progress in x-ray sources and x-ray optical components has facilitated the utilization of CDSAXS within the semiconductor industry. Compared to stationary and rotating anode microfocus x-ray sources, liquid-metal jet x-ray sources emit x-ray beams with higher energy and higher flux. Their brightness can rival that of second-generation synchrotron radiation light sources [21], rendering them feasible for high-throughput in-line measurements. Concerning x-ray optical components, customized multilayer mirrors have the capacity to focus the beam on the sample, thereby diminishing the required size of overlay target and ensuing measurement efficiency.

Conclusion. Our proposal introduces x-ray-based overlay metrology using RSS. We derive a linear relationship that combines the overlay and scattering intensities, subsequently optimizing the measurement configurations for optimal results. The simulation results validate the method's efficacy and illustrate its robustness against potential errors arising from the overlay target grating fabrication and the measurement process. It is worth noting that, in contrast to prevailing x-ray-based nanostructure metrology which necessitate RSM and address the inverse problem, our proposed method employing RSS holds the potential to substantially reduce the measurement time and would be suitable for in-line measurements. Furthermore, RSS proposed here also shows the latent capacity for the emerging diffraction-based overlay metrology employing soft x-ray and extreme ultraviolet wavelengths [22]. It is crucial to emphasize that this study represents the initial validation of the proposed method. The future research will span both theoretical and experimental domains. We will scrutinize more intricate sources of noise and error and conduct thorough parameter correlation and sensitivity analysis.

Funding. National Natural Science Foundation of China (52022034, 62175075, 52130504).

Disclosures. The authors declare no conflicts of interest.

Data availability. Data underlying the results presented in this paper are not publicly available at this time but may be obtained from the authors upon reasonable request.

Supplemental document. See Supplement 1 for supporting content.

REFERENCES

1. B. W. Smith and K. Suzuki, *Microlithography Science and Technology*, 3rd ed. (CRC Press, 2020), Chap. 12.
2. International Roadmap for Devices and Systems (IRDS), Metrology (Table MET-3) (2022), https://irds.ieee.org.
3. W. Yang, R. L. Webb, S. Rabello, *et al.*, Proc. SPIE **5038**, 200 (2003).
4. C. Messinis, T. T. M. van Schaijk, N. Pandey, *et al.*, Opt. Express **28**, 37419 (2020).
5. A. J. den Boef, Surf. Topogr.: Metrol. Prop. **4**, 023001 (2016).
6. X. Chen, J. Hu, W. Chen, *et al.*, Opt. Lett. **48**, 3383 (2023).
7. X. Chen, H. Gu, H. Jiang, *et al.*, Opt. Express **25**, 8491 (2017).
8. N. G. Orji, M. Badaroglu, B. M. Barnes, *et al.*, Nat. Electron. **1**, 532 (2018).
9. T. Hu, R. L. Jones, W. L. Wu, *et al.*, J. Appl. Phys. **96**, 1983 (2004).
10. D. F. Sunday and R. J. Kline, J. Micro/Nanolithogr., MEMS, MOEMS **17**, 1 (2018).
11. D. F. Sunday, S. List, J. S. Chawla, *et al.*, J. Appl. Crystallogr. **48**, 1355 (2015).
12. A. F. Hannon, D. F. Sunday, D. Windover, *et al.*, J. Micro/Nanolithogr., MEMS, MOEMS **15**, 034001 (2016).
13. A. Veldman, M. S. Bakeman, A. V. Shchegrov, *et al.*, "Methods and apparatus for measuring semiconductor device overlay using X-ray metrology," U.S. patent 9,885,962B2 (6 February, 2018).
14. S. P. Zeuschner, M. Mattern, J. E. Pudell, *et al.*, Struct. Dyn. **8**, 014302 (2021).
15. D. F. Sunday, F. Delachat, A. Gharbi, *et al.*, J. Appl. Crystallogr. **52**, 106 (2019).
16. H. C. Hsieh, J. M. Cheng, and Y. C. Yeh, Appl. Opt. **61**, 1389 (2022).
17. Y. Shi, K. Li, X. Chen, *et al.*, Appl. Opt. **59**, 2897 (2020).
18. C. T. Liu, B. C. He, G. D. Chen, *et al.*, Nanomaterials **10**, 1549 (2020).
19. W. E. Fu, B. C. He, and W. L. Wu, Surf. Topogr.: Metrol. Prop. **11**, 024008 (2023).
20. W. E. Fu and W. L. Wu, "Apparatus for amplifying intensity during transmission small angle—X-ray scattering measurements," U.S. patent 9,297,772B2 (29 March, 2016).
21. M. Wansleben, C. Zech, C. Streeck, *et al.*, J. Anal. At. Spectrom. **34**, 1497 (2019).
22. C. L. Porter, T. Coenen, N. Geypen, *et al.*, Proc. SPIE **12496**, 50 (2023).

115.156.143.240 {ts '2023-12-05 22:30:57'}

Supplemental Document

Optics Letters

X-ray-based overlay metrology using reciprocal space slicing analysis: supplement

JIAHAO ZHANG,[1] XIUGUO CHEN,[1,2,*] TIANJUAN YANG,[1] AND SHIYUAN LIU[1,2]

[1] *State Key Laboratory of Intelligent Manufacturing Equipment and Technology, Huazhong University of Science and Technology, Wuhan 430074, China*
[2] *Optics Valley Laboratory, Wuhan 430074, China*
[*] *xiuguochen@hust.edu.cn*

This supplement published with Optica Publishing Group on 5 December 2023 by The Authors under the terms of the Creative Commons Attribution 4.0 License in the format provided by the authors and unedited. Further distribution of this work must maintain attribution to the author(s) and the published article's title, journal citation, and DOI.

Supplement DOI: https://doi.org/10.6084/m9.figshare.24498283

Parent Article DOI: https://doi.org/10.1364/OL.505346

X-ray-based overlay metrology using reciprocal space slicing analysis: supplemental document

1. Theoretical framework of X-ray-based overlay metrology using reciprocal space slicing

The form factor of overlay target grating with symmetrical and the same trapezoidal cross-section is

$$F\left(q_x,q_z\right)=\left(\Delta\rho_1+\Delta\rho_2 e^{-\mathrm{i}\left(q_x\cdot OV+q_z S\right)}\right)F_{trap}\,. \tag{S1}$$

The scattering intensity is expressed as the square of the modulus of this form factor

$$\begin{aligned}I\left(q_x,q_z\right)&=\left|F\left(q_x,q_z\right)\right|^2=\left|F_{trap}\right|^2\cdot\left|\Delta\rho_1+\Delta\rho_2 e^{-\mathrm{i}\left(q_x\cdot OV+q_z S\right)}\right|^2\\&=\left|F_{trap}\right|^2\cdot\left[\Delta\rho_1+\Delta\rho_2\cdot\left(\cos Z-i\sin Z\right)\right]\cdot\left[\Delta\rho_1+\Delta\rho_2\cdot\left(\cos Z+i\sin Z\right)\right],\\&=\left|F_{trap}\right|^2\cdot\left[\left(\Delta\rho_1+\Delta\rho_2\cos Z\right)^2+\left(\Delta\rho_2\sin Z\right)^2\right]\end{aligned} \tag{S2}$$

where $Z=q_x\cdot OV+q_z S$. Due to OV being a relatively small quantity, expand the above equation in Taylor series at $Y=q_z S$ and omit the higher orders,

$$\begin{cases}\sin Z=\sin Y+\cos Y\cdot q_x\cdot OV\\ \cos Z=\cos Y-\sin Y\cdot q_x\cdot OV\end{cases}. \tag{S3}$$

For ideal target grating without overlay, the scattering intensity is

$$I_0\left(q_x,q_z\right)=\left|F_{trap}\right|^2\cdot\left[\left(\Delta\rho_1+\Delta\rho_2\cos Y\right)^2+\left(\Delta\rho_2\sin Y\right)^2\right]=\left|F_{trap}\right|^2\cdot\left(A^2+B^2\right). \tag{S4}$$

Relative fluctuations in scattering intensity can be expressed as

$$\begin{aligned}\frac{I\left(q_x,q_z\right)-I_0\left(q_x,q_z\right)}{I_0\left(q_x,q_z\right)}&=\frac{\left(A-\Delta\rho_2\sin Y\cdot q_x\cdot OV\right)^2+\left(B+\Delta\rho_2\cos Y\cdot q_x\cdot OV\right)^2-\left(A^2+B^2\right)}{A^2+B^2}\\&\approx\frac{-2A\cdot\Delta\rho_2\sin Y\cdot q_x\cdot OV+2B\cdot\Delta\rho_2\cos Y\cdot q_x\cdot OV}{A^2+B^2}\\&=2\Delta\rho_2\frac{A\sin Y-B\cos Y}{A^2+B^2}q_x\cdot OV\\&=K\left(\Delta\rho_1,\Delta\rho_2,q_x,q_z,S\right)\cdot OV\end{aligned}, \tag{S5}$$

where we omit the quadratic terms containing OV and $A=\Delta\rho_1+\Delta\rho_2\cos Y, B=\Delta\rho_2\sin Y$.

When introducing a set of designed shifts ±d to the overlay target, apply Eq. (S5) to the shifts ±d:

$$\begin{cases} \dfrac{I_{OV+d}\left(q_x,q_z\right)-I_d\left(q_x,q_z\right)}{I_d\left(q_x,q_z\right)}=-2\Delta\rho_2\dfrac{A_+\sin M-B_+\cos M}{A_+^2+B_+^2}q_x\cdot OV=K_1\left(\Delta\rho_1,\Delta\rho_2,q_x,q_z,S,d\right)\cdot OV \\ \dfrac{I_{OV-d}\left(q_x,q_z\right)-I_{-d}\left(q_x,q_z\right)}{I_{-d}\left(q_x,q_z\right)}=-2\Delta\rho_2\dfrac{A_-\sin N-B_-\cos N}{A_-^2+B_-^2}q_x\cdot OV=K_2\left(\Delta\rho_1,\Delta\rho_2,q_x,q_z,S,-d\right)\cdot OV \end{cases},\tag{S6}$$

where $M=+q_x d+q_z S, N=-q_x d+q_z S$ and

$$\begin{cases} A_+=\Delta\rho_1+\Delta\rho_2\cos M \\ B_+=\Delta\rho_2\sin M \\ A_-=\Delta\rho_1+\Delta\rho_2\cos N \\ B_-=\Delta\rho_2\sin N \end{cases}.\tag{S7}$$

The distinct relationship between the scattering intensities at +d and −d is

$$K_3=\frac{I_{+d}}{I_{-d}}=\frac{\left|\Delta\rho_1+\Delta\rho_2 e^{-\mathrm{i}\left[q_x d+q_z S\right]}\right|^2}{\left|\Delta\rho_1+\Delta\rho_2 e^{-\mathrm{i}\left[q_x(-d)+q_z S\right]}\right|^2}=\frac{A_+^2+B_+^2}{A_-^2+B_-^2}.\tag{S8}$$

According to Eq. (S6) and (S8), the formula for measuring overlay can be obtained as

$$OV=\frac{I_{OV+d}\left(q_x,q_z\right)-K_3 I_{OV-d}\left(q_x,q_z\right)}{K_1 K_3 I_{OV-d}\left(q_x,q_z\right)-K_2 I_{OV+d}\left(q_x,q_z\right)}.\tag{S9}$$

2. Other simulation results

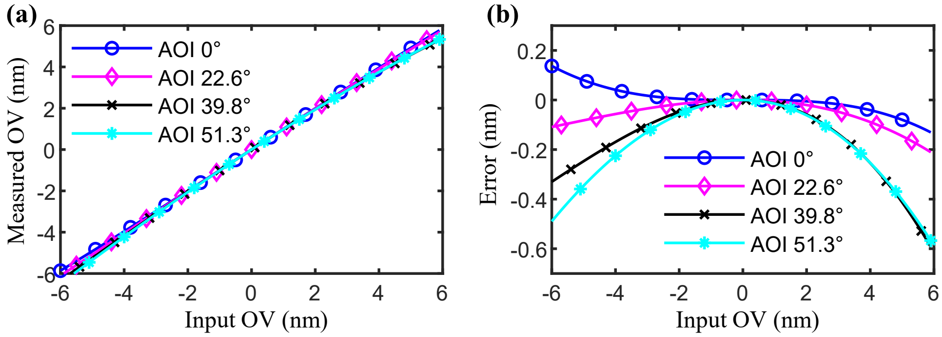

Fig.S1 Measured overlay (a) and the corresponding errors (b) with errors of thickness of the silicon dioxide filling layer for optimized AOI.

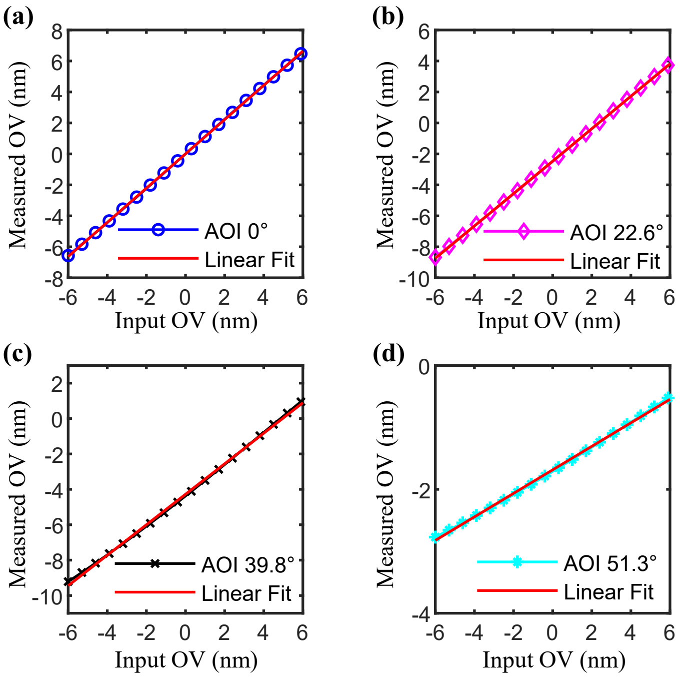

Fig.S2 Measured overlay in the presence of cross-sectional fabrication discrepancies for optimized AOI.

Table S1. Fitting results of the linear relationship between Input OV (IOV) and Measured OV (MOV) in the presence of cross-sectional error.

AOI	Fitted linear expression (MOV=a×IOV+b)		Coefficient of determination R^2
	Slope a	Intercept b (nm)	
0°	1.1054	5.3×10^{-4}	0.99996
22.6°	1.0463	–2.4675	0.99996
39.8°	0.8611	–4.2766	0.99913
51.3°	0.1898	–1.6856	0.99892

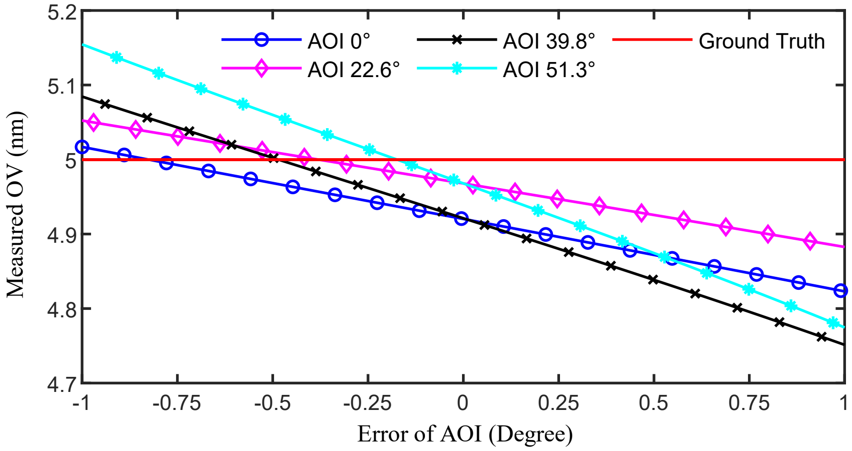

Fig.S3 Measured overlay in the presence of errors of AOI.

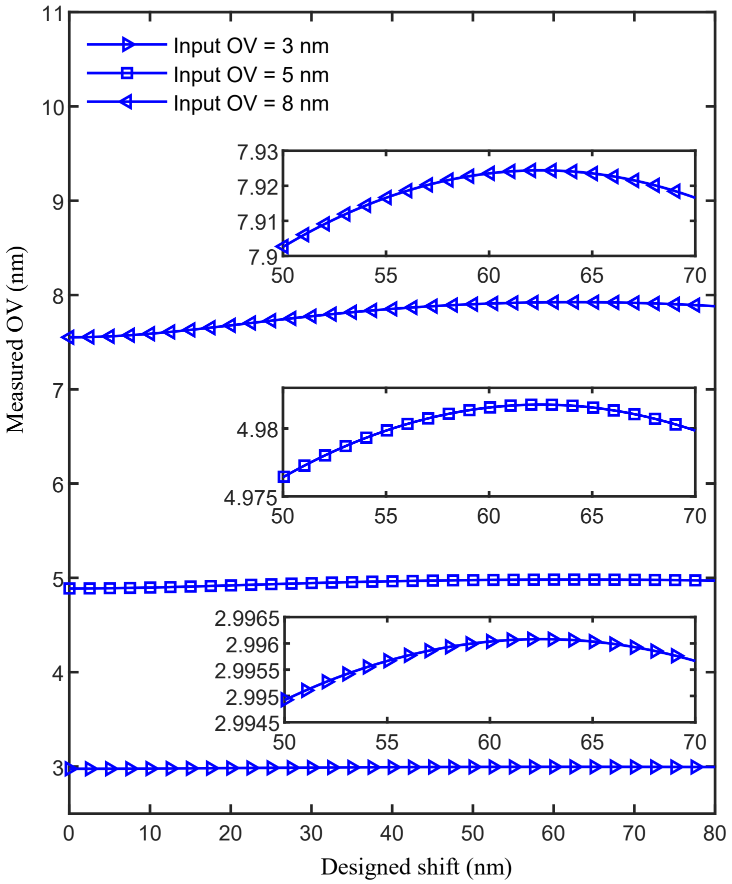

Fig.S4 Measured overlay with different designed shift of the overlay target grating, where input overlays are fixed at 3 nm, 5 nm and 8 nm, respectively. Insets show the measured overlay when the designed shift ranges from 50 nm to 70 nm, all being the most accurate at the designed shift equal to 62.5 nm.